



# Liquid-like condensates mediate competition between actin branching and bundling

Kristin Graham<sup>a</sup> , Aravind Chandrasekaran<sup>b</sup>, Liping Wang<sup>c</sup>, Noel Yang<sup>a</sup>, Eileen M. Lafer<sup>c</sup>, Padmini Rangamani<sup>b,1</sup> , and Jeanne C. Stachowiak<sup>a,d,1</sup>

Edited by Sandra Schmid, Chan Zuckerberg Biohub, San Francisco, CA; received May 31, 2023; accepted November 21, 2023

Cellular remodeling of actin networks underlies cell motility during key morphological events, from embryogenesis to metastasis. In these transformations, there is an inherent competition between actin branching and bundling, because steric clashes among branches create a mechanical barrier to bundling. Recently, liquid-like condensates consisting purely of proteins involved in either branching or bundling of the cytoskeleton have been found to catalyze their respective functions. Yet in the cell, proteins that drive branching and bundling are present simultaneously. In this complex environment, which factors determine whether a condensate drives filaments to branch or become bundled? To answer this question, we added the branched actin nucleator, Arp2/3, to condensates composed of VASP, an actin bundling protein. At low actin to VASP ratios, branching activity, mediated by Arp2/3, robustly inhibited VASP-mediated bundling of filaments, in agreement with agent-based simulations. In contrast, as the actin to VASP ratio increased, addition of Arp2/3 led to formation of aster-shaped structures, in which bundled filaments emerged from a branched actin core, analogous to filopodia emerging from a branched lamellipodial network. These results demonstrate that multi-component, liquid-like condensates can modulate the inherent competition between bundled and branched actin morphologies, leading to organized, higher-order structures, similar to those found in motile cells.

biomolecular condensate | liquid-liquid phase separation | cytoskeleton | actin | biomechanics

The cellular cytoskeleton is organized into numerous higher-order structures that achieve diverse physiological functions. Specifically, the actin cytoskeleton can be organized into parallel or antiparallel bundles, branched networks, or crosslinked networks, each conferring different mechanical properties that are optimized for specific cellular processes (1–3). Cell motility relies on the combined efforts of these different morphologies to enable propulsion of the cell's leading edge, central contraction, and subsequent retraction of the cell's trailing edge. The leading edge comprises both parallel actin bundles, found in finger-like filopodial protrusions, and branched actin networks, found in the sheet-like lamellipodium (4). Assembly of branched actin networks requires the branch nucleator, Arp2/3, which, upon activation by Wiskott–Aldrich syndrome protein (WASP)-family proteins, binds to the sides of mother actin filaments, nucleating a branch (5, 6). Interestingly, assembly of parallel bundles of actin filaments, found in filopodia, is thought to originate from an underlying branched actin network. Specifically, processive actin polymerases, such as formins or Ena/VASP proteins, are thought to catalyze the convergent elongation of linear filaments that originate from the branched actin network of the lamellipodium (7, 8). With assistance from crosslinkers like fascin, these parallel bundles can become rigid enough to bend the plasma membrane, leading to protrusions (9).

We have recently shown that the processive actin polymerase, VASP, forms liquid-like droplets that polymerize actin filaments and organize them into parallel bundles, similar to filopodia (10). This process is mediated by competition between the rigidity of the filaments and the surface tension of the droplet, along with VASP's ability to crosslink filaments. Droplet-mediated bundling of actin occurs through a series of morphological transitions and symmetry-breaking events. Specifically, as actin polymerizes, it forms a three-dimensional shell within the droplet, which collapses into a two-dimensional ring as actin polymerization continues. As the ring accumulates more actin and thickens, its increasing bending rigidity eventually overcomes the surface tension of the droplet, deforming the droplet into a disc. Deformation into a disc is concomitant with droplet elongation into higher aspect ratio structures, which eventually form rods. The resulting rods appear to be composed of parallel bundles of actin filaments, consistent with VASP's cellular function in mediating parallel bundling of linear actin filaments.

Interestingly, recent work from other groups has shown that liquid-like condensates of TPX2 are capable of nucleating microtubule branches (11). Taken together, these

## Significance

Reorganization of actin filaments allows cells to migrate, which is required for embryonic development, wound healing, and cancer metastasis. During migration, the leading edge of the cell consists of needle-like protrusions of bundled actin, which emanate from a sheet of branched actin. Given that the proteins responsible for both architectures are present simultaneously, what determines whether actin filaments will be branched or bundled? Here, we show that liquid-like condensates, composed of both branching and bundling proteins, can mediate the inherent competition between these fundamentally different ways of organizing actin networks. This work demonstrates that by tuning the composition of condensates, we can recapitulate the transition from branched to bundled networks, a key step in cell migration.

Author contributions: K.G., A.C., P.R., and J.C.S. designed research; K.G., A.C., L.W., N.Y., E.M.L., P.R., and J.C.S. performed research; K.G., A.C., L.W., and E.M.L. contributed new reagents/analytic tools; K.G., A.C., N.Y., P.R., and J.C.S. analyzed data; and K.G., A.C., P.R., and J.C.S. wrote the paper.

The authors declare no competing interest.

This article is a PNAS Direct Submission.

Copyright © 2024 the Author(s). Published by PNAS. This article is distributed under [Creative Commons Attribution-NonCommercial-NoDerivatives License 4.0 \(CC BY-NC-ND\)](https://creativecommons.org/licenses/by-nc-nd/4.0/).

<sup>1</sup>To whom correspondence may be addressed. Email: [prangamani@ucsd.edu](mailto:prangamani@ucsd.edu) or [jcstach@austin.utexas.edu](mailto:jcstach@austin.utexas.edu).

This article contains supporting information online at <https://www.pnas.org/lookup/suppl/doi:10.1073/pnas.2309152121/-/DCSupplemental>.

Published January 11, 2024.

studies suggest that liquid-like condensates can be harnessed to facilitate the two major organizing mechanisms within filament networks: bundling and branching. Furthermore, one study revealed that the formation of branched actin networks by Arp2/3 can inhibit the formation of fascin-induced actin bundles (12). Thus, given the potential for both competition and cooperation between these mechanisms of organization, we wondered how condensates might modulate network morphology when the protein machinery required for bundling and branching are present simultaneously. Specifically, because VASP has been found to drive actin polymerization in plasma membrane clusters in the lamellipodia, as well as in the tips of filopodia, we reasoned that VASP condensates provide an ideal platform to investigate both branching and bundling behaviors (7, 13–15).

How might the introduction of a branched actin network impact the bundling activity of the VASP droplets? Here, we show that Arp2/3 can be added to VASP droplets to create branched actin networks within the droplets. As expected, droplets that contain a branched network are less likely to deform into linear structures. Specifically, we found that droplets with more Arp2/3, and therefore more branched actin, are arrested at an initial step in the bundling process. Agent-based modeling of filament dynamics suggests that this effect results from Arp2/3's ability to reduce the effective length of filaments, making it more difficult for them to become bundled close to droplet periphery. However, as the actin concentration increased, filament networks transitioned from a branched to a bundled state, deforming droplets into aster-shaped structures consisting of a central hub from which thin, actin-filled spokes emanated. Interestingly, Arp2/3 segregated spontaneously to the hubs of these asters and was simultaneously depleted from the spokes, demonstrating actin-mediated partitioning of protein components within droplets. This work illustrates how liquid-like condensates of actin-interacting proteins could modulate the competing processes of actin branching and bundling, critical steps in cytoskeletal dynamics throughout the cell.

## Results

**Arp2/3 and VCA Participate in Phase Separation of Liquid-like VASP Droplets.** To investigate the impact of the branched actin nucleator, Arp2/3, on droplet-mediated bundling of actin filaments, we began by incorporating Arp2/3 into droplets composed of VASP. Specifically, we formed droplets of 20  $\mu\text{M}$  VASP (monomer concentration; 5  $\mu\text{M}$  of VASP tetramer) in the presence of Arp2/3, and its activator, the VCA domain of N-WASP. Droplets are formed by mixing VASP and associated proteins with the crowding agent PEG8000, to a final concentration of 3% (w/v). VASP is a native tetramer (16, 17). However, we hereafter refer to the monomeric concentration of VASP so that the actin-to-VASP ratios more intuitively reflect the ratio between actin and actin-binding sites on VASP. Phase-separated condensates have been shown to localize proteins through both specific and nonspecific interactions (18–20). To visualize whether VASP droplets were capable of localizing Arp2/3 and VCA, we formed VASP droplets in the presence of fluorescently labeled Arp2/3 and VCA. Arp2/3 was labeled with maleimide Atto-594 (21), and VCA was labeled with maleimide Atto-488 (5). Both proteins were enriched in VASP droplets (Fig. 1*A*). While VASP has been found to bind the proline-rich domain of some WASP-family proteins, there are no known interactions of VASP with the N-WASP VCA domain (22–24). Similarly, Arp2/3 lacks known VASP interaction motifs. Therefore, enrichment of these proteins in VASP droplets is likely driven by nonspecific or weak binding interactions, which can appear amplified in concentrated droplet systems (19, 25). Since both Arp2/3 and the VCA domain

of WASP natively participate in electrostatic interactions in the cell, we anticipate that these residues may contribute to nonspecific electrostatic interactions with VASP (26–29). While addition of Arp2/3 had little effect on VASP droplets, addition of the VCA fragment resulted in VASP droplets with a distribution of larger diameters in comparison to droplets consisting of VASP alone (Fig. 1*B* and *C*). This effect, which suggests that VCA reinforces condensation of VASP, could result from non-specific interactions between acidic residues in the VCA fragment with basic residues in VASP (16, 28–31). Furthermore, the seemingly larger impact of VCA on VASP droplets compared to Arp2/3 could be attributed to the excess VCA relative to Arp2/3, which we used to mimic previous *in vitro* actin branching assays (27–31). Importantly, VASP droplets formed with Arp2/3 and VCA remained liquid-like, fusing rapidly upon contact (Fig. 1*D*). Composite droplets of VASP, Arp2/3, and VCA also exhibited recovery after photobleaching that was comparable to that of droplets consisting of VASP alone (Fig. 1*E* and *F*). Composite droplets exhibited a slightly slower recovery rate, with a  $\tau_{1/2}$  of  $7.24 \pm 0.99$  s, compared to a  $\tau_{1/2}$  of  $4.93 \pm 1.16$  s for VASP-only droplets, suggesting that the presence of VCA and Arp2/3 may increase the degree of protein-protein interaction within droplets (Fig. 1*E*, *Bottom*). However, the fraction of mobile VASP was not significantly changed upon addition of Arp2/3 and VCA (Fig. 1*E*, *Bottom*). Overall, these data indicate that VASP droplets formed with Arp2/3 and VCA maintain liquid-like physical properties.

**Addition of Arp2/3 and VCA to VASP Droplets Inhibits Droplet Deformation and Actin Bundling.** We next sought to test how branched actin nucleators might alter droplet-mediated bundling of actin filaments. We added 2  $\mu\text{M}$  of actin monomers (labeled with maleimide Atto-488) to pre-formed VASP droplets (15  $\mu\text{M}$ , labeled with maleimide AlexaFluor 647), with increasing concentrations of Arp2/3 and VCA. For each tested concentration of Arp2/3, we maintained the Arp2/3 to VCA ratio constant at 1:40, which is within the range used in the literature (20, 32–35). After allowing the actin to polymerize for 15 min, after which minimal changes to droplet phenotype are observed (10), the droplets were imaged. As expected from previous work (10), VASP droplets lacking Arp2/3 and VCA deformed into rod-like shapes upon actin polymerization (Fig. 2*A*). However, as the fraction of Arp2/3 and VCA increased, the droplets became more spherical, and their overall aspect ratios decreased (Fig. 2*A* and *B*). Importantly, actin still polymerized into filaments in the presence of Arp2/3 and VCA, as confirmed with phalloidin staining (Fig. 2*C*). Notably, phalloidin-stained actin frequently arranged into rings at the inner surfaces of droplets, as observed previously (10).

Smaller droplets are more likely to deform at a given actin concentration because growing actin filaments have to bend more tightly to fit inside them (10). Therefore, we asked whether the slight increase in droplet size owing to inclusion of VCA and Arp2/3 (Fig. 1*C*) could explain the reduction in droplet aspect ratio in Fig. 2*A* and *B*. To answer this question, we reanalyzed the data in Fig. 2*A* and *B* for droplets with a minor axis below 3  $\mu\text{m}$ , the average size of droplets consisting of VASP alone. Similar to the full population, we observed a substantial reduction in aspect ratio with increasing Arp2/3 concentration for droplets below this threshold (Fig. 2*D*). This result confirms that increased droplet size cannot explain the reduction in droplet deformation in the presence of VCA and Arp2/3. Collectively, these data demonstrate that, despite continuing to drive actin polymerization, inclusion of Arp2/3 and VCA in VASP droplets greatly reduces the ability of polymerized actin filaments to deform VASP droplets and generate bundled-actin structures.

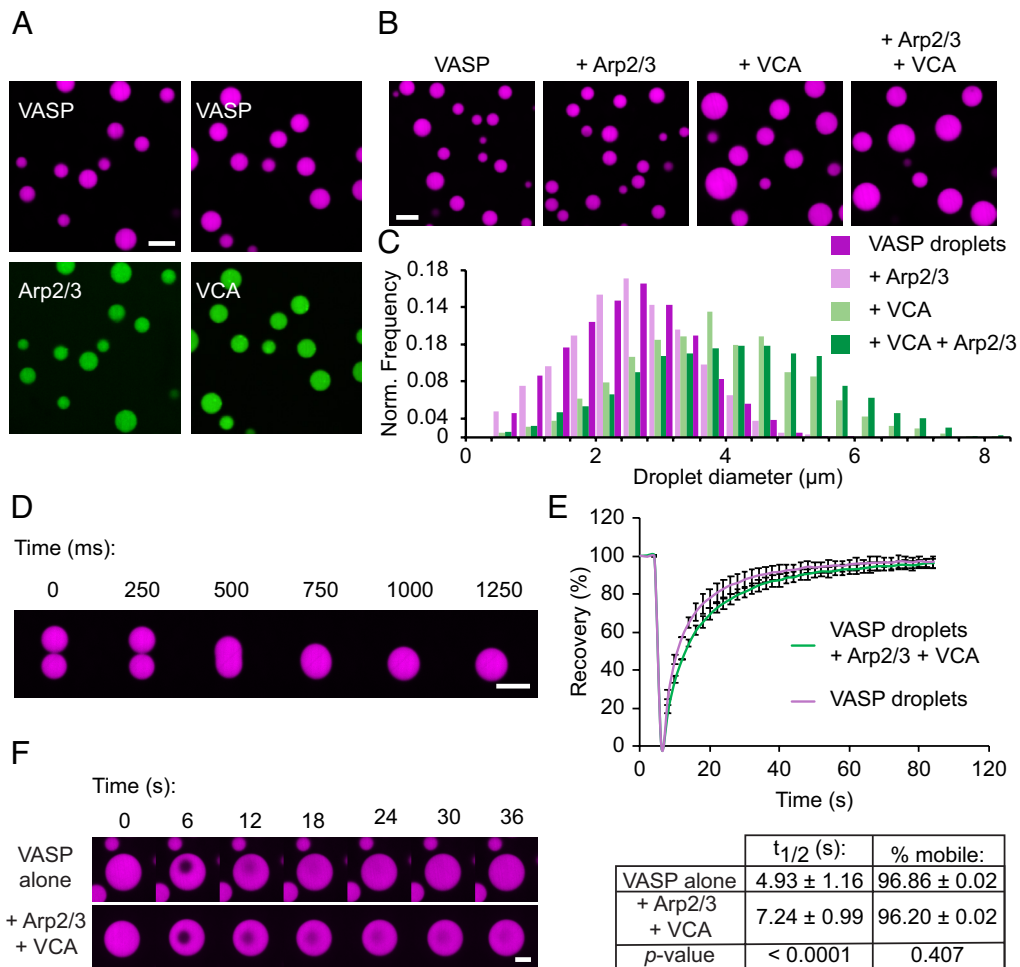


**Fig. 1.** Arp2/3 and VCA participate in phase separation of liquid-like VASP droplets. (A) Enrichment of 1  $\mu\text{M}$  Arp2/3 (labeled with Atto-594, shown in green) or 1  $\mu\text{M}$  VCA (labeled with Atto-488, shown in green) to 20  $\mu\text{M}$  VASP droplets. Droplets are formed in “droplet buffer”: 50 mM Tris pH 7.4, 150 mM NaCl, 3% (w/v) PEG8000. (Scale bar, 5  $\mu\text{m}$ .) (B) Representative images of droplets formed from a 20  $\mu\text{M}$  solution of VASP with either 150 nM Arp2/3, 6  $\mu\text{M}$  VCA, or both 150 nM Arp2/3 and 6  $\mu\text{M}$  VCA. (Scale bar, 5  $\mu\text{m}$ .) (C) Histogram of droplet sizes quantified from B. Data from  $n = 3$  replicates. (D) Composite droplets formed of 20  $\mu\text{M}$  VASP, 150 nM Arp2/3, and 6  $\mu\text{M}$  VCA still remain liquid-like, as exhibited by rapid fusion events. (Scale bar, 5  $\mu\text{m}$ .) (E) Composite droplets formed of 20  $\mu\text{M}$  VASP, 150 nM Arp2/3, and 6  $\mu\text{M}$  VCA display rapid recovery after photobleaching, and the fraction of mobile VASP is nearly equivalent to droplets lacking Arp2/3 and VCA. Curves show the average VASP recovery profile with error bars representing SD for  $n = 13$  droplets for each condition. Inset table shows  $t_{1/2}$  and percent mobile fraction for each condition, with corresponding  $P$ -values from an unpaired two-tailed  $t$ -test. (F) Representative time series of FRAP of either VASP-only droplets, or composite droplets as quantified in E. (Scale bar, 2  $\mu\text{m}$ .)

The experiments in Fig. 2 *A–D* examined relatively large VASP droplets for which actin polymerization drives relatively small changes in droplet aspect ratio. To determine whether inclusion of Arp2/3 and VCA can also inhibit larger actin-driven deformations, we titrated the same concentrations of Arp2/3 in smaller droplets formed at a VASP concentration of 5  $\mu\text{M}$ , rather than 15  $\mu\text{M}$ . Actin was added to these droplets at a concentration of 0.67  $\mu\text{M}$  to maintain the same actin to VASP ratio of 1:7.5 (Fig. 2*E*). The concentration of VCA was 4  $\mu\text{M}$ . In the absence of Arp2/3, actin polymerization within these smaller droplets resulted in rod-like structures with some aspect ratios exceeding 20 (Fig. 2*E*, *Left*). However, addition of as little as 50 nM of Arp2/3 resulted in a dramatic decrease in the aspect ratio (Fig. 2*E* and *F*). In particular, the number of droplets with aspect ratios substantially above 2 decreased upon introduction of even 50 nM Arp2/3, which is 100-fold lower than the VASP concentration of 5  $\mu\text{M}$ . These results further demonstrate that branched filaments resulting from Arp2/3 and VCA present a barrier to filament bundling and thus inhibit the deformation of spherical droplets into higher aspect ratio structures (Fig. 2*G*).

**Decreased Droplet Deformation Is due to the Combined Effect of Arp2/3 and VCA.** We next investigated the molecular mechanisms by which Arp2/3 and VCA inhibited actin bundling. The first possibility we considered was that a reduction in actin partitioning to VASP droplets in the presence of Arp2/3 and VCA resulted in less actin polymerization within droplets and therefore a reduction in high aspect ratio structures. A reduction in partitioning could occur if Arp2/3 and VCA were to compete with actin for space within the crowded droplet environment. To evaluate this idea, we used the data in Fig. 2 *A* and *B* to plot the droplet aspect ratio as a function of the actin intensities inside the droplets, Fig. 3*A*. This plot demonstrates that the aspect ratio declines substantially with increasing Arp2/3 concentration, even when droplets with the same actin intensity are compared. These results indicate that steric exclusion of actin from VASP droplets in the presence of Arp2/3 and VCA cannot explain the loss of high aspect ratio structures and likely does not occur to a substantial degree.

We next sought to determine whether the ability of Arp2/3 and VCA to nucleate assembly of branched actin networks could explain the reduction in droplet aspect ratio. Since Arp2/3 is

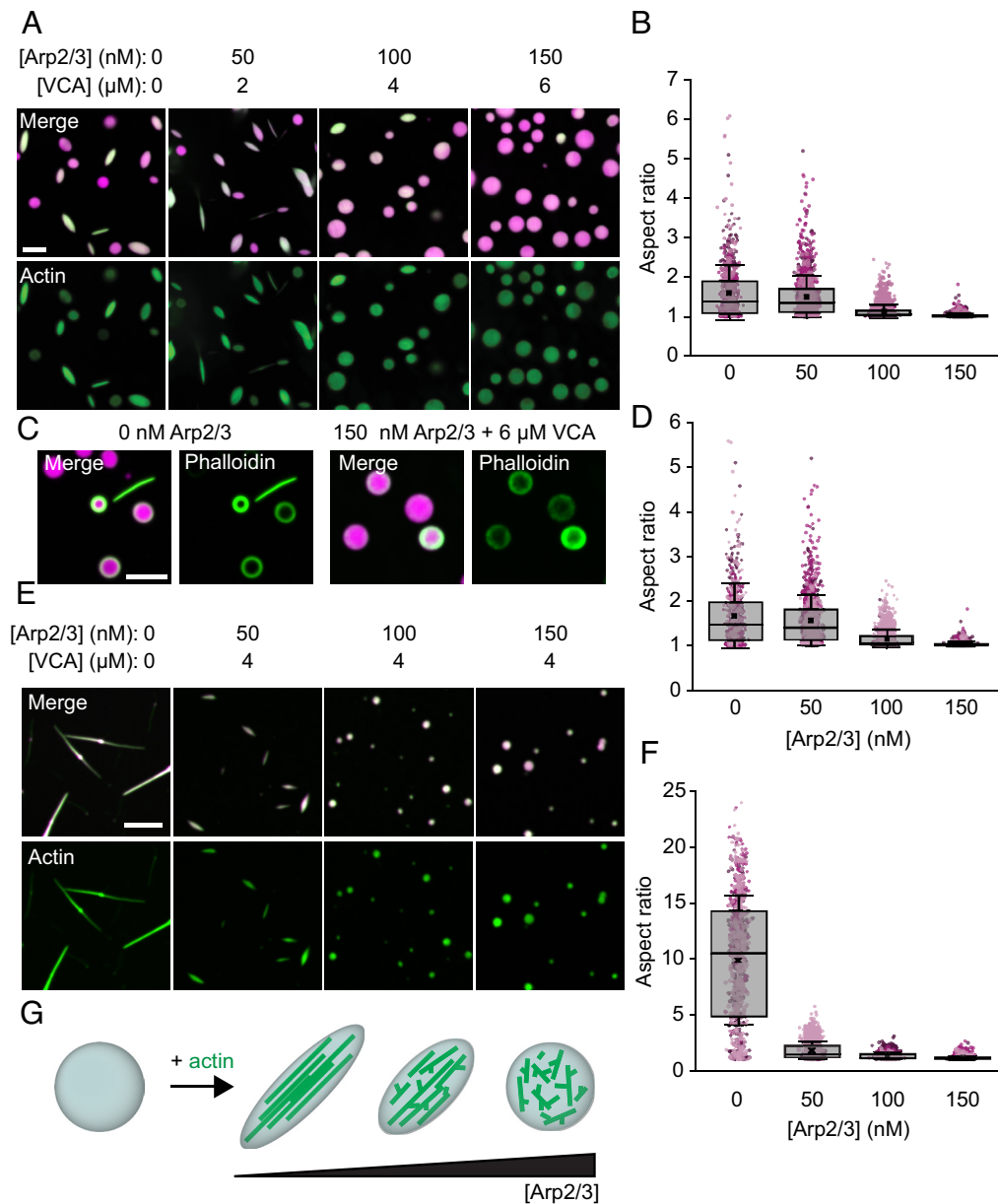


**Fig. 2.** Addition of Arp2/3 and VCA to VASP droplets inhibits droplet deformation and actin bundling. (A) Representative images of droplets formed from 15  $\mu\text{M}$  VASP and 2  $\mu\text{M}$  actin, with increasing concentrations of Arp2/3 and VCA. (Scale bar, 5  $\mu\text{m}$ .) (B) Quantification of aspect ratios of droplets in A. Box represents interquartile range (IQR) with median as a bisecting line, mean as an “x,” and whiskers, which represent SD. Each background color point represents a single droplet, and are color-coded according to the three replicates. For 0 nM Arp2/3,  $n = 755$  droplets; for 50 nM Arp2/3,  $n = 1,391$ ; for 100 nM Arp2/3,  $n = 2,123$ ; for 150 nM Arp2/3,  $n = 2,286$ . (C) Representative images of phalloidin staining of 2  $\mu\text{M}$  actin polymerized by either 15  $\mu\text{M}$  VASP-only droplets, or 15  $\mu\text{M}$  VASP droplets with 150 nM Arp2/3 and 6  $\mu\text{M}$  VCA. (Scale bar, 5  $\mu\text{m}$ .) (D) Quantification of aspect ratios of droplets in B, filtered for droplets with a minor axis  $< 3 \mu\text{m}$ . For 0 nM Arp2/3,  $n = 653$  droplets; for 50 nM Arp2/3,  $n = 1,105$ ; for 100 nM Arp2/3,  $n = 1,232$ ; for 150 nM Arp2/3,  $n = 1,040$ . (E) Representative images of droplets formed from 5  $\mu\text{M}$  VASP, exposed to 0.67  $\mu\text{M}$  actin, with 4  $\mu\text{M}$  VCA and increasing concentrations of Arp2/3. (Scale bar, 5  $\mu\text{m}$ .) (F) Quantification of droplet aspect ratio as a function of Arp2/3 concentration as seen in E. The box represents IQR with median as a bisecting line, mean as an x, and whiskers, which represent SD. Data from three replicates. For 0 nM Arp2/3,  $n = 656$ ; for 50 nM Arp2/3,  $n = 1,116$ ; for 100 nM Arp2/3,  $n = 1,239$ ; for 150 nM Arp2/3,  $n = 1,006$ . (G) Cartoon depicting sphere-to-rod transition driven by the ability of VASP droplets to bundle actin filaments, a process which is inhibited by the addition of Arp2/3 and VCA.

activated by the N-WASP VCA domain, we tested the impact of omitting VCA on droplet aspect ratio, Fig. 3B. The resulting droplets, which contained inactive Arp2/3, had a comparable distribution of aspect ratios to those consisting only of VASP and actin, demonstrating that activation of Arp2/3 is required for the decrease in aspect ratio (Fig. 3B and C). We next tested the impact of N-WASP’s VCA domain on droplet deformation in the absence of Arp2/3. Interestingly, the addition of VCA to droplets consisting of VASP and actin resulted in a decrease in droplet aspect ratio, although not as substantial as when combined with Arp2/3 (Fig. 3B and C). The VCA fragment has been previously shown

to inhibit actin filament nucleation and elongation in the absence of Arp2/3, which may explain these observations (36). In line with this idea, reducing the concentration of VCA from 6  $\mu\text{M}$  to 750 nM reduced VCA’s ability to suppress droplet deformation in the absence of Arp2/3. Under these conditions, Arp2/3 activity, activated by VCA, appears to be the dominant mechanism of aspect ratio suppression (Fig. 3D and E). This result suggests that both (i) Arp2/3 mediated-branching activity and (ii) sequestration of actin by VCA contribute to the decreased aspect ratios observed. However, the importance of Arp2/3 activity is highlighted in Fig. 2E and F, where VCA remains constant and increasing

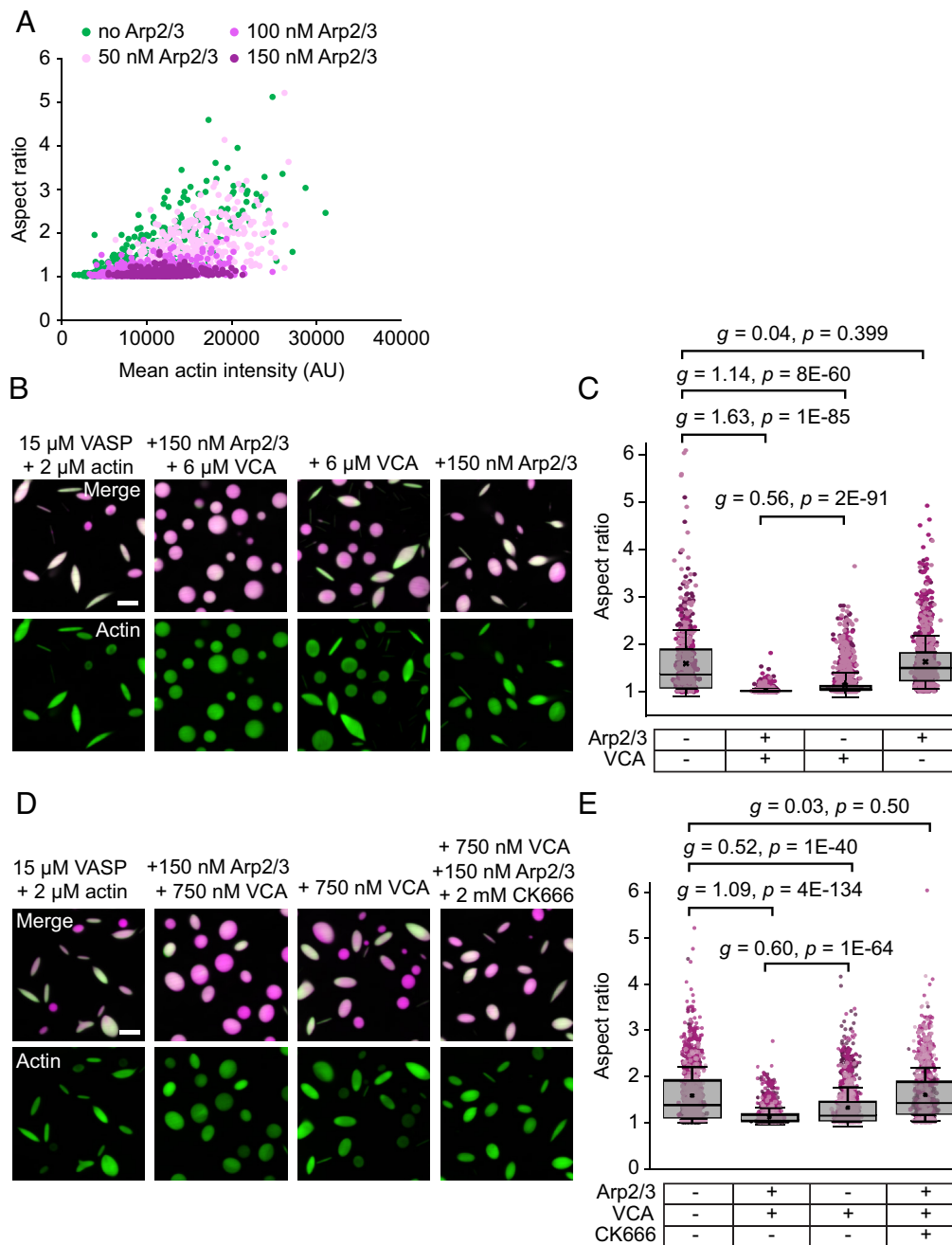


**Fig. 3.** Decreased droplet deformation is due to Arp2/3 and VCA. (A) Relationship between droplet aspect ratio and actin intensity within the droplet for droplets formed from 15  $\mu$ M VASP and exposed to 2  $\mu$ M actin with increasing concentrations of Arp2/3 and VCA, as visualized in Fig. 2A. Replicates can be found in *SI Appendix, Fig. S1*.  $n = 2,885$  droplets counted over at least three images per condition. (B) Representative images of droplets composed of 15  $\mu$ M VASP and 2  $\mu$ M actin, with either i) 150 nM Arp2/3 and 6  $\mu$ M VCA added, ii) only VCA, or iii) only Arp2/3. (Scale bar, 5  $\mu$ m.) (C) Quantification of droplet aspect ratio measured from B. Box represents IQR with median as a bisecting line, mean as an x, and whiskers represent SD. Data points are color-coded according to three independent replicates. At least 700 droplets were analyzed per condition. Brackets show data tested for effect size using Hedges'  $g$ , and significance using an unpaired two-tailed  $t$ -test. (D) Representative images of droplets composed of 15  $\mu$ M VASP and 2  $\mu$ M actin, with either i) 150 nM Arp2/3 and 750 nM VCA added, ii) only VCA, or iii) Arp2/3, VCA, and the Arp2/3 inhibitor, CK666. (Scale bar, 5  $\mu$ m.) (E) Quantification of droplet aspect ratio measured from D. The box represents IQR with median as a bisecting line, mean as an x, and whiskers represent SD. Data points are color-coded according to three independent replicates. At least 1,000 droplets were analyzed per condition. Brackets show data tested for effect size using Hedges'  $g$ , and significance using an unpaired two-tailed  $t$ -test.

Arp2/3 concentrations result in further aspect ratio reductions. Therefore, to further elucidate the role of actin branching, we assayed droplets of VASP, Arp2/3, VCA, and actin in the presence of the Arp2/3 inhibitor, CK666 (37, 38). Similar to the absence of VCA, inhibition of Arp2/3 by CK666 resulted in a distribution of aspect ratios similar to those of droplets consisting only of VASP and actin (Fig. 3 D and E and *SI Appendix, Fig. S2*). Importantly, since the most significant difference was observed for 6  $\mu$ M VCA with 150 nM Arp2/3, we used this 40:1 ratio of VCA to Arp2/3

for the remainder of the studies in this paper. Together, these data show that VCA and activated Arp2/3, which is known to drive assembly of branched actin networks (35, 39) are responsible for the decrease in aspect ratio of droplets.

**Arp2/3 Activity Reduces Droplet Deformation by Inhibiting Assembly of Actin Rings.** We next sought to determine the mechanism by which Arp2/3 activity inhibits droplet deformation. For this purpose, we examined the architecture of actin filaments

within droplets. First, we repeated the experiment in Fig. 2A, but stained with phalloidin, which specifically binds to actin filaments, rather than directly labeling actin monomers (Fig. 4A). Our previous work showed that when actin polymerizes in droplets consisting only of VASP, actin filaments frequently partition to the inner periphery of droplets, where their curvature is minimized (10). In contrast, we found that, as the Arp2/3 and VCA fraction increased, actin filaments were less likely to adopt peripheral actin distributions, instead being distributed throughout the droplet (Fig. 4A and B). Specifically, we found that droplets with an increased fraction of

Arp2/3 and VCA showed less accumulation of actin at the inner surfaces of droplets (Fig. 4B). Further, Arp2/3 and VCA containing droplets that displayed peripheral actin accumulation tended to have a more diffuse, “fuzzy” appearance (Fig. 4C). More quantitatively, as the concentration of Arp2/3 increased, actin partitioning to the periphery was reduced, leaving a higher concentration of actin in the interior of the droplet (Fig. 4C and D).

In droplets consisting of VASP alone, once actin filaments accumulate at the droplet periphery, they spontaneously rearrange into a planar ring that gradually overcomes the droplet surface tension,

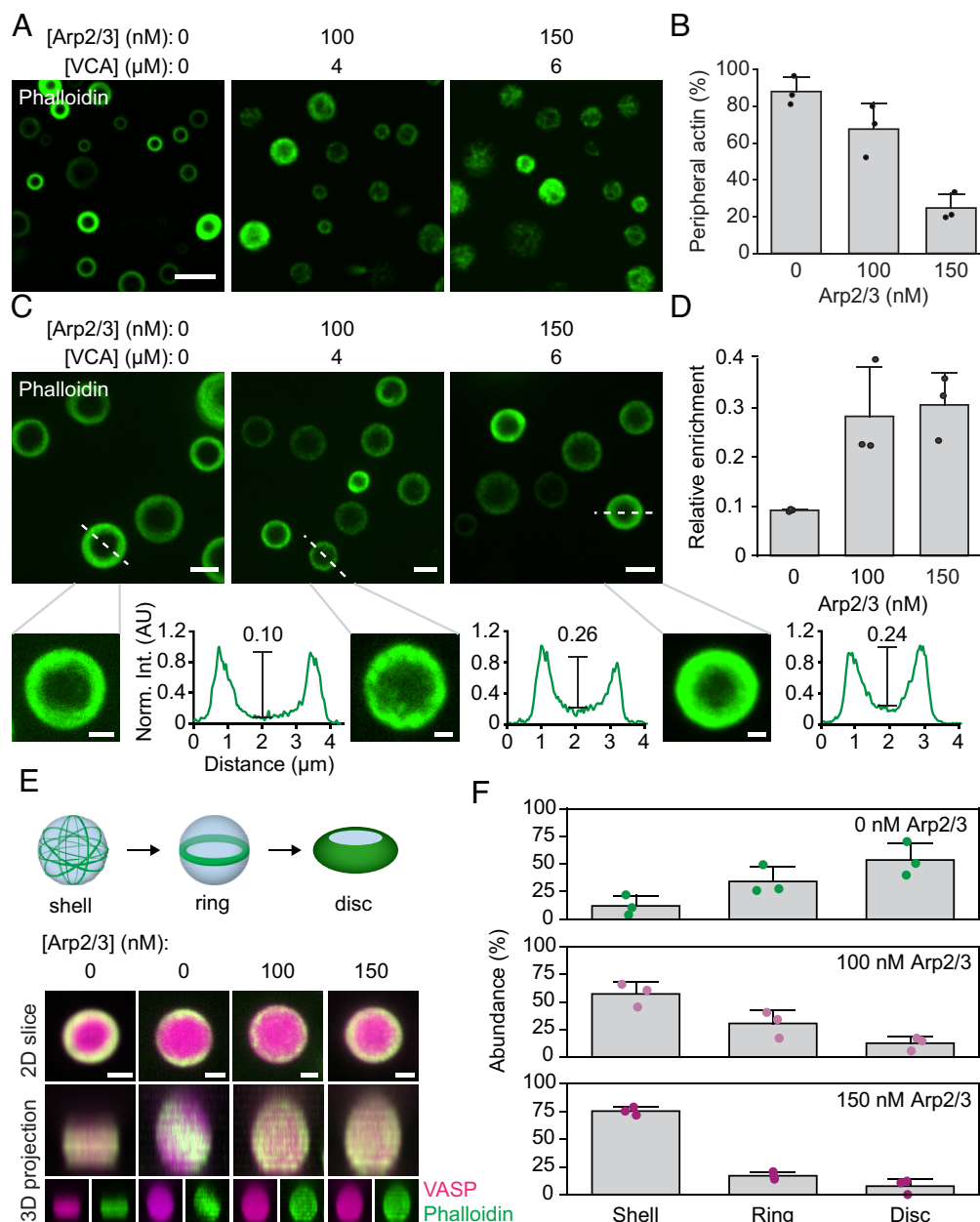


**Fig. 4.** Arp2/3 activity reduces droplet deformation by inhibiting assembly of actin rings. (A) Representative images of droplets formed from 15 μM VASP with 2 μM actin and increasing concentration of Arp2/3 and VCA, stained with phalloidin. (Scale bar, 5 μm.) (B) Quantification of the abundance of droplets with peripheral actin accumulation as a function of Arp2/3 concentration. Bars represent mean ± SD of n = 3 experiments, with three images analyzed per condition. (C, Top) Representative images of droplets formed as in A, exhibiting peripheral accumulation of actin filaments. (Scale bar, 2 μm.) Bottom: Line profiles of actin intensity in designated droplets. The calculated enrichment of actin in the droplet center is displayed above a line that estimates the relative height difference between the droplet center and periphery, which is analogous to the enrichment calculation in D. (Scale bar, 1 μm.) Actin intensities are normalized to the max intensity of each profile. Note that the contrast was adjusted in the zoomed-in inserts to better display the relative intensities in the center of the droplet to the periphery. (D) Quantification of the relative enrichment of actin to the interior of the droplet compared to the periphery. Data are mean ± SD from n = 3 experiments, with 12 droplets analyzed per condition. (E, Top) Cartoon of the different 3D spatial arrangements of droplets with peripheral actin. Bottom: Representative 3D projections of droplets as in C, revealing examples of disc, ring, and shell distributions of actin. (Scale bar, 1 μm.) (F) Distribution of the abundance of actin shells, rings, and discs in droplets formed from 15 μM VASP with 2 μM actin and increasing Arp2/3 and VCA concentrations as shown in A–D. Bars are mean ± SD across n = 3 experiments, with 3 images analyzed per condition. Statistical analysis is shown in SI Appendix, Fig. S3.

flattening spherical droplets into discs (Fig. 4 *E*, *Top*) (10). We analyzed 3D reconstructions of the data in Fig. 4 *A* and *C* to determine the impact of Arp2/3 and VCA on these transitions. The reconstructed images show that as the concentration of Arp2/3 increased, droplets mainly contained peripheral actin “shells”, which largely failed to condense into two-dimensional rings and discs (Fig. 4 *E* and *F* and *SI Appendix*, Fig. S3). The resulting distribution of rings and discs can be attributed to variations in actin concentration within each droplet, given our previous observation that actin concentration controls the relative probabilities of assembling shells, rings, or discs of actin within droplets (10). These data indicate that Arp2/3 activity inhibits the rearrangement of actin filaments into the higher-order structures required for droplet deformation. Specifically, a decrease in assembly of actin rings would fundamentally undermine droplet deformation and actin bundling. Without the bundling of actin into more compact and rigid structures, the droplet is less likely to deform into an elongated shape.

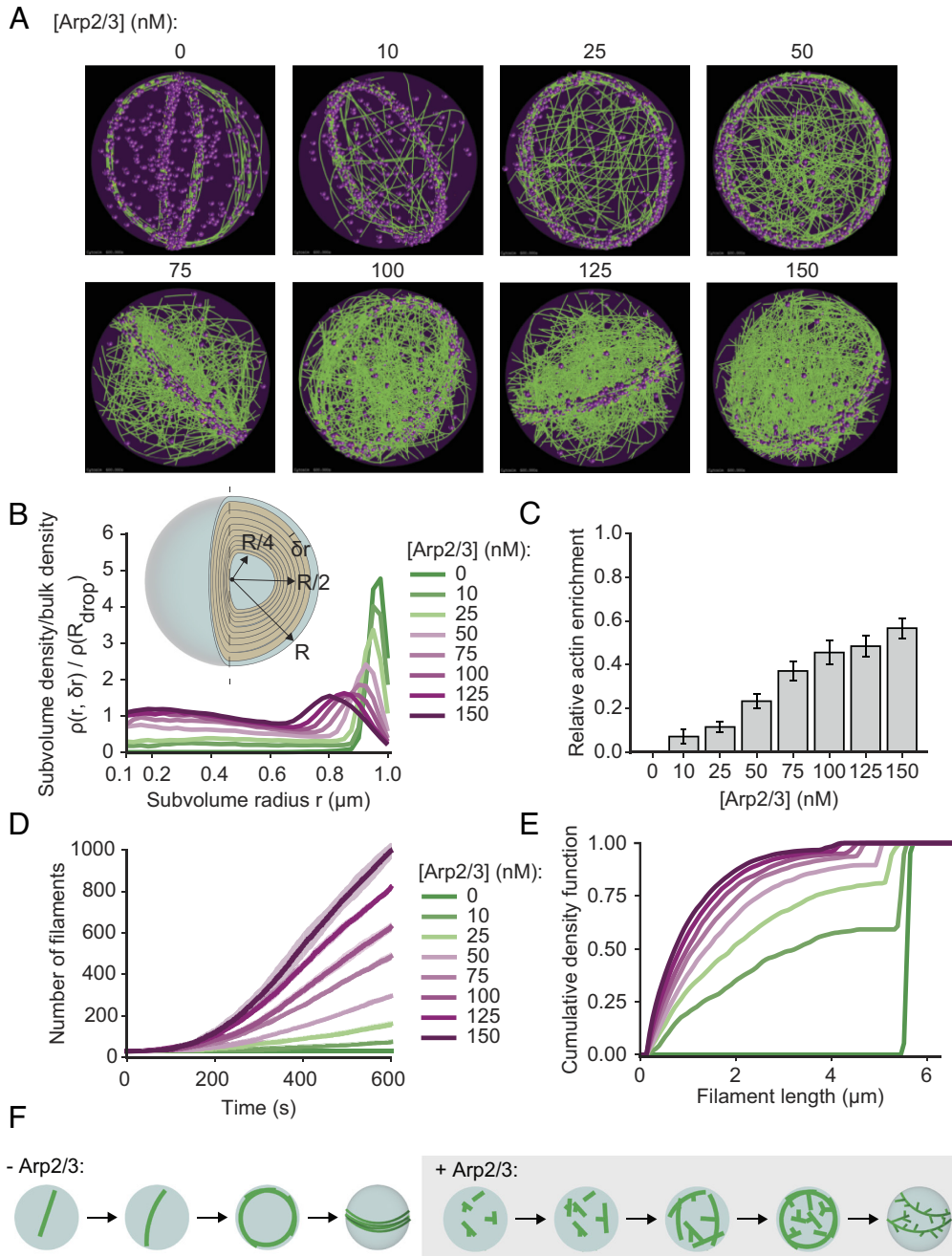
**Simulations Suggest that Filament Branching Inhibits the Formation of Actin-rich Rings by Reducing the Average Length of Filaments.** Our experiments demonstrate that Arp2/3 activity is responsible for inhibiting assembly of actin-rich rings inside VASP droplets, but they do not resolve the changes in the morphology of the actin network that are responsible for this inhibition. To gain greater insight into these phenomena, we used Cytosim, an agent-based framework for modeling cytoskeletal dynamics (35), to perform mechanochemical simulations of actin networks within droplets with a fixed radius of 1  $\mu\text{m}$ . To capture their mechanical deformability, actin filaments were discretized into a series of segments that were allowed to bend along hinge points (*SI Appendix*, Fig. S4). Actin, VASP, and Arp2/3 molecules were constrained within the boundary of spherical droplets using harmonic potentials (*SI Appendix*, Fig. S4). Additionally, spatial overlap between filaments and VASP molecules was prevented by applying steric potentials (*SI Appendix*, Fig. S4). Chemical evolution of the network in Cytosim involved actin filament growth, binding, and unbinding of VASP to actin, and binding of Arp2/3 to actin, resulting in nucleation of filament branches (*SI Appendix*, Fig. S4). The simulations also accounted for Brownian dynamics of the molecules considered. While kinetic parameters for Arp2/3 were chosen from experimental data (*SI Appendix*, Table S1), kinetic parameters for VASP were chosen based on simulations of actin polymerization within VASP droplets that lacked Arp2/3 (36). The present simulations are described in detail in the *SI Appendix*, *Methods*, Fig. S4, and Table S1.

Fig. 5*A* shows snapshots of the simulation after 10 min, which provided sufficient time for the distribution of actin inside the droplets to approach steady state. In the absence of Arp2/3, actin rings form at the inner periphery of the droplets, in agreement with experimental results (Fig. 4*E*). However, as the concentration of Arp2/3 increased, we observed an increasing number of actin filaments within the droplet that were not part of the ring. Specifically, at Arp2/3 concentrations above 100 nM, the actin distribution within the droplet became largely homogenous. To determine the radial distribution of F-actin within the droplet, we discretized the volume into a series of overlapping shells of finite thickness (25 nm). Computing the ratio of local F-actin density to the bulk F-actin density for each of these shells, we observed that the ring configuration in the absence of Arp2/3 displayed a marked accumulation of actin at the periphery of the droplet and was devoid of actin elsewhere (Fig. 5*B*). As the concentration of Arp2/3 increased, we observed three distinct regions within the droplets, each of which had different actin distributions. Near the

center of the droplet ( $r \leq 0.1 \mu\text{m}$ ) the density ratio was dominated by small volume effects and is therefore not depicted in Fig. 5*B*. In the droplet core ( $0.2 \leq r < 0.6$ ), we observed a steady increase in the density ratio as the concentration of Arp2/3 increased, which is summarized in Fig. 5 *B* and *C*. Finally, in the droplet periphery ( $r \geq 0.6$ ), we observed a marked decrease in actin accumulation. These distinct behaviors can be understood by looking at changes in the characteristics of the filaments with increasing Arp2/3 concentration. Specifically, Fig. 5*D* shows that increasing the concentration of Arp2/3 resulted in enhanced nucleation of actin filaments throughout the trajectory. As a result, the median filament length decreased, resulting in an increasing number of filaments with lengths below the droplet diameter (Fig. 5*E*). These shorter filaments do not have to bend to remain within the confines of the droplet, and as a result, their driving force to partition to the droplet periphery is greatly reduced (Fig. 5*F*). We also studied the role of VCA by modeling VCA as a chemical species that competes for actin, without explicitly resolving VCA molecules. The details of the VCA model and the parameters used are explained in *SI Appendix*, *Methods*. Simulating networks at various concentrations of Arp2/3 and VCA, we observed that VCA competes for actin monomers, resulting in reduced filament length and a subtle reduction in the number of filaments nucleated (*SI Appendix*, Fig. S5 *A* and *B*). As the resulting shorter filaments cannot be bundled effectively, VCA did not alter overall network morphology at the concentrations used in our experiments (*SI Appendix*, Fig. S6 and *Movie S4*).

Taken together, the results of our experiments (Fig. 4) and simulations (Fig. 5) suggest that the ability of filament branching to undermine ring formation can be explained by two key phenomena. First, branches increase the effective diameter of filaments, sterically inhibiting filament bundling within rings. This finding is consistent with previous studies of actin-Arp2/3 interactions (40, 41). Second, branched actin filaments are shorter, on average, than unbranched filaments, because the actin monomers within the branch are unavailable to add to the length of the mother filament. The resulting shorter filaments cannot exert sufficient forces to overcome the surface tension of the droplet. Specifically, when the length of filaments exceeds the droplet diameter, filaments must bend to remain within the droplet. Because the persistence length of actin,  $\sim 17 \mu\text{m}$  (42), is greater than the diameter of most of the droplets in our experiments (10) (Fig. 1*C*), this bending comes at a substantial energetic cost that can be minimized by partitioning filaments to the inner droplet surface, where their curvature is lowest (43). Since branched filaments are fundamentally shorter, they will be less likely to encounter this constraint, when compared to longer, linear filaments.

**At High Actin-to-VASP Ratios, Arp2/3 Activity Drives Aster-like Morphologies.** Up to this point, our data indicate that for relatively low actin to VASP ratios, Arp2/3 activity strongly inhibits droplet-mediated actin bundling. In particular, results from experiments, further elucidated by simulations, suggest that Arp2/3 activity results in an abundance of short, branched filaments that fail to deform droplets. Similarly, prior work has shown that branching and bundling proteins compete with one another when the supply of actin is limited (44). Together, these results suggest that a limited supply of actin may be inhibiting droplet deformation in our experiments. Based on this reasoning, we next explored the impact of increasing the actin concentration in our system. Specifically, we added increasing concentrations of Arp2/3 to droplets formed at higher actin to VASP ratios, beginning with a 1:1 ratio (5  $\mu\text{M}$  VASP and 5  $\mu\text{M}$  actin), holding VCA concentration constant at 4  $\mu\text{M}$  (Fig. 6*A*). At Arp2/3 concentrations as low as 50 nM, the



**Fig. 5.** Simulations predict that Arp2/3-driven changes to filament length distribution inhibit the formation of actin-rich rings at the droplet periphery. (A) Representative final snapshots ( $t = 600$  s) from rigid droplets (radius =  $1 \mu\text{m}$ ) [VASP-tet] =  $0.2 \mu\text{M}$  and various Arp2/3 concentrations are shown. Actin filaments are shown in green while VASP tetramers are shown as magenta spheres. [Movie S3](#) shows the time evolution of the trajectories. (B) Plot shows the mean ratio of actin density within subvolume shells of radius  $r$  and thickness  $\delta r = 25$  nm (shown in *Inset*) to the overall density of actin within the droplet of radius  $R$ . Plot lines are colored based on Arp2/3 concentration. *Inset* depicts subvolume shells, with shells of radius  $r = R/4$ ,  $R/2$ , and  $R$  highlighted, with  $0 \leq r \leq R$ . (C) Actin enrichment close to droplet core is calculated as defined in *SI Appendix, Methods* as the ratio of maximum actin density at the core ( $0.2 \leq r_c < 0.6$ ) and periphery ( $0.6 \leq r_c < 1.0$ ). Data from six replicates; the last 10 snapshots per replicate were used here. (D) Mean (solid line) and SD (shaded area) in the number of actin filaments are plotted as time traces and colored based on the concentration of Arp2/3. (E) The final distribution of filament lengths (last 10 snapshots per replicate) is plotted as a cumulative density function and colored by Arp2/3 concentration. Data from five replicates. (F) Proposed model describing ring formation in the absence and presence of Arp2/3 activity.

VASP droplets began to deform into forked structures, which we did not observe at the lower actin to VASP ratios used in Fig. 2. These forked structures increased in abundance as the Arp2/3 concentration increased.

Next, we further increased the actin to VASP ratio to 4:1 ( $1 \mu\text{M}$  VASP and  $4 \mu\text{M}$  actin), again, gradually increasing the concentration of Arp2/3, while holding VCA concentration constant at  $4 \mu\text{M}$  (Fig. 6B). At this actin to VASP ratio, multi-pronged, three-dimensional, aster-like structures emerged with increasing

Arp2/3 concentration (Fig. 6C and D). These droplet-mediated asters appear similar to previously reported actin asters, which formed on beads coated with WASP, Arp2/3, and fascin, an actin bundling protein (45). In these previous studies, Arp2/3 at the surface of the bead nucleated a branched actin network, which was then bundled by fascin to form radiating spokes. Similar results have also been observed in the absence of beads, in which actin self-assembled into asters in the presence of VCA, Arp2/3, and fascin (34, 46, 47). Importantly, our system lacks fascin.



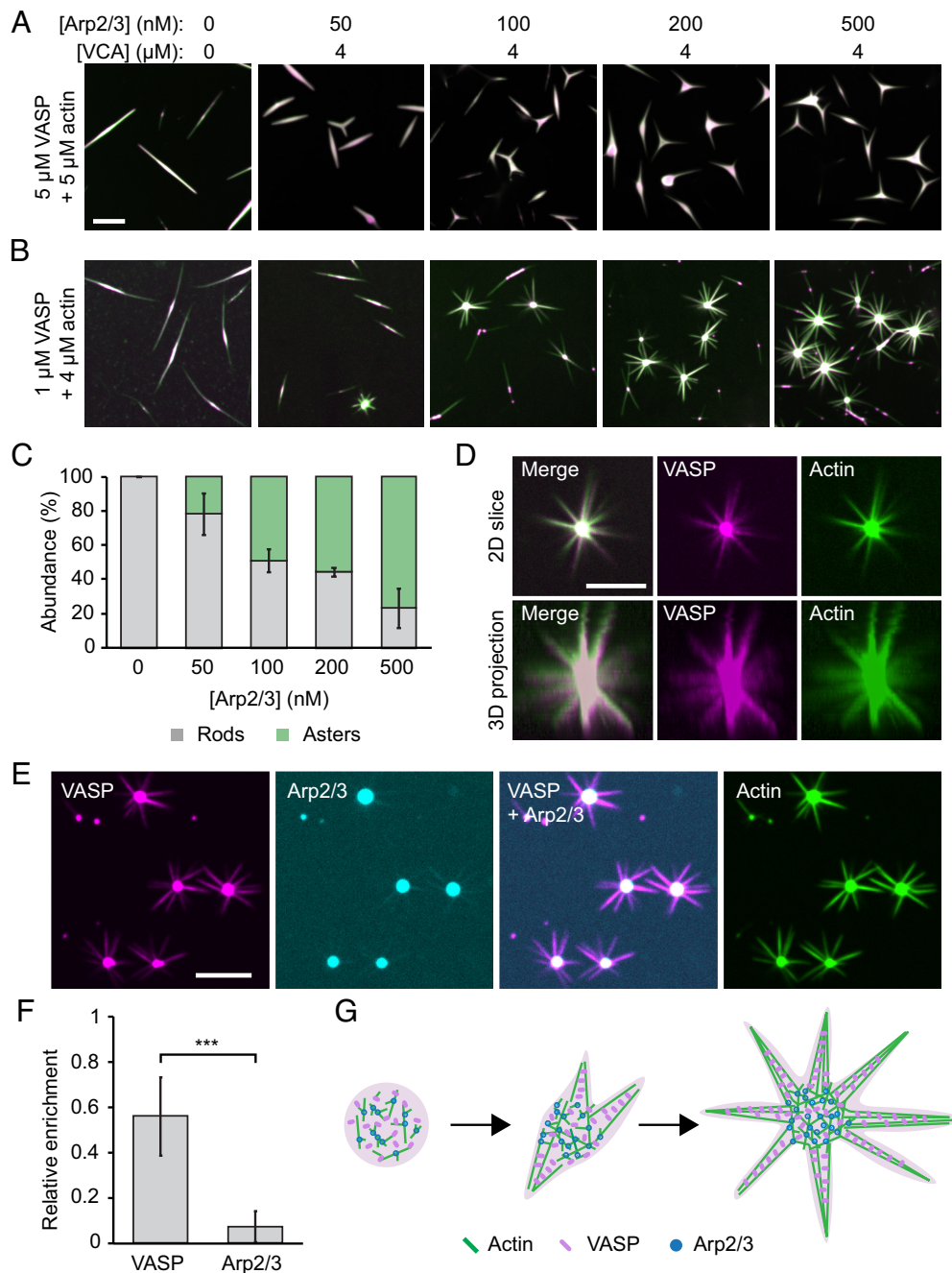


**Fig. 6.** At high actin-to-VASP ratios, Arp2/3 activity drives aster-like morphologies. (A) Titration of Arp2/3 and 4 μM VCA in droplets formed from 5 μM VASP and exposed to 5 μM actin. (Scale bar, 5 μm.) (B) Titration of Arp2/3 and 4 μM VCA as in A into droplets formed from 1 μM VASP and exposed to 4 μM actin. (Scale bar, 5 μm.) (C) Quantification of the percent of droplets that deformed into rods and asters in B. Bars are mean ± SD across n = 3 experiments, with at least four images analyzed per condition. (D) 3D projection of a representative aster-shaped droplet. (Scale bar, 5 μm.) (E) Representative images of VASP, Arp2/3, and actin intensity distributions throughout aster-shaped droplets. Condition: 1 μM VASP, 500 μM Arp2/3, 4 μM VCA, 4 μM actin. (Scale bar, 5 μm.) (F) Quantification of the relative enrichment of VASP and Arp2/3 to the spokes of aster-shaped droplets. Enrichment is normalized to actin intensity. Droplets formed as in E. Bars are mean ± SD across n = 3 experiments, with 10 droplets analyzed per experiment. Asterisks indicates data tested for significance via an unpaired two-tailed t-test, with  $P < 0.001$ . (G) Proposed model for Arp2/3- and VASP-mediated aster formation.

However, because VASP is a tetramer, it is able to crosslink actin filaments, such that it acts as a bundling protein (17, 48).

Interestingly, in droplet-mediated asters, we found that VASP colocalized with actin in both the droplet core and along the spokes, while Arp2/3 was mainly localized to the droplet core and depleted from the spokes (Fig. 6E and F). Specifically, comparison of the spoke to core intensity ratio for VASP and Arp2/3 showed that VASP's relative partitioning to the spokes was nearly 10-fold greater than Arp2/3's (partitioning of  $6.8 \pm 2.3\%$  compared to  $0.69 \pm 0.52\%$  mean ± SD) (Fig. 6F). This result suggests that

branched actin structures are more likely to exist in the core of the asters, while the spokes likely consist of more linear filaments, bundled by VASP, Fig. 6G. In this way, the protein droplet, which consists of VASP, Arp2/3 and VCA, mediates the segregation of branched and bundled actin networks.

## Discussion

We have previously shown that liquid-like protein droplets consisting of VASP can catalyze the polymerization of actin and its assembly into parallel bundles (10). In the present work, we show

that creation of a branched actin network, through the activity of Arp2/3 and VCA, competes with the filament bundling activity of VASP. In particular, at low actin to VASP ratios, introduction of Arp2/3 and VCA resulted in potent inhibition of droplet bundling, such that droplets remained spherical (Fig. 2). The resulting branched network of filaments failed to break symmetry, forming a relatively homogenous actin mesh within the droplets, rather than accumulating at the droplet periphery (Figs. 4 and 5). Computational modeling suggested that this lack of filament partitioning to the droplet periphery is due to a reduction in filament length, as well as an increase in steric hindrance among branched filaments. Guided by these results, we found that at higher actin to VASP ratios, bundles emerged from the droplets, resulting in aster-like morphologies. Importantly, since cells naturally maintain high actin to VASP ratios, the formation of asters could parallel cellular branch-to-bundle transitions (49, 50).

Interestingly, recent work showed that, when Arp2/3 and actin are co-encapsulated in vesicles, actin branching suppresses fascin-mediated bundling (12). This observation was attributed to competition between fascin and Arp2/3 for a limited supply of actin. This competition may parallel the competition that we have observed between VASP, Arp2/3, and VCA. Specifically, when the concentration of actin in our droplet system increased, bundling re-emerged, resulting in forked and aster-like structures. These structures likely formed because the increased actin concentration allowed the growth of longer actin filaments, which are more easily bundled. Interestingly, VASP was enriched in the spokes of these structures, while Arp2/3 was enriched in their cores, further suggesting that the spokes consisted primarily of bundled actin, which emerged from a branched actin core. This observation parallels prior studies that have reported the spontaneous formation of actin asters in the presence of Arp2/3, WASP, and fascin (34, 45, 46). In all systems, a branched actin core, rich in Arp2/3, gave rise to bundled filaments that were rich in actin bundling proteins—either fascin or VASP. Importantly, a liquid-like state could enhance aster formation by concentrating actin monomers, as we observed asters at lower actin concentrations than previous studies (34, 45).

How does an actin bundle emerge from a network of branched filaments? One hypothesis is that actin filaments, nucleated by Arp2/3, need to reach a critical length before they can become bundled (34, 51). Specifically, filaments need to be long enough to bend toward each other so that they can be crosslinked by a bundling protein, such as VASP (34). Longer filaments would likely concentrate at the droplet periphery, where their curvature is minimized. Assembly of these peripheral filaments into bundles could explain the aster-like morphologies that we observe (Fig. 6). Additionally, the droplet's surface tension may enhance bundling by opposing filament branching, similar to previous observations in reconstituted membrane systems (52). In this way, the mechanics of the droplet could promote the emergence of actin bundles that originate from a branched actin interior.

At the leading edge of the cell, the sheet-like lamellipodium is filled with a branched actin network that relies on Arp2/3-mediated nucleation (53). Filopodia, finger-like membrane protrusions rich in bundled actin, emerge from the lamellipodium through the action of actin polymerases, as well as bundling proteins. Growth of filopodia requires that long, unbranched filaments emerge from the branched lamellipodium (4, 8). VASP has been shown to assist in this process by i) processively elongating filaments, ii) clustering barbed ends, and iii) bundling filaments (48, 54–56). Importantly, VASP localizes to the tips of filopodia (13, 57, 58). In this way, filopodia are enriched in VASP and depleted of Arp2/3, which parallels the segregation of VASP and Arp2/3 in our droplet-mediated asters. While we recognize that our simple *in vitro* experiment lacks

the complexity and additional components found in the cytoplasm, this finding suggests that protein condensation could play a role in mediating branch-to-bundle transitions of the cytoskeleton (Fig. 6G).

Overall, this work suggests roles for phase separation in the organization of the cytoskeleton. The cellular leading edge is inherently dynamic, owing to the continual rearrangement of the membrane, actin, and associated machinery. Importantly, Arp2/3 and WASP-family proteins have been found to participate in protein condensation (20, 32, 33), and oligomerization of WASP-family proteins synergistically increases their activity (59, 60). Thus, since VCA is enriched within the droplets, we might expect enhanced nucleation activity due to its increased local concentration and potential to synergistically enhance activity of nearby VCA molecules. However, the impact of phase separation on the exact conformation and activities of Arp2/3 and VCA are unknown and remain a point of future research. VASP has also been shown to form dynamic clusters on the lamellipodial membrane that exhibit fusion and fission (15), and clustering of VASP enhances its processivity as an actin polymerase (54). Fusion of these VASP clusters results in fusion and bundling of their associated filaments before filopodia formation (15). Thus, the capillary forces arising from a liquid could enhance bundling in addition to conventional biochemical crosslinking, generating thicker, more rigid bundles that may assist in the formation of plasma membrane protrusions. Finally, VASP has also recently been shown to form protein-rich phases on planar membrane substrates that drive actin filament bundling (61). While the role of protein condensation in the cytoskeleton is still emerging, these results collectively suggest multiple mechanisms by which condensates could participate in network remodeling. In particular, our work suggests that, by tuning the composition of condensates, cytoskeletal networks can dictate the assembly of branched or bundled architectures.

## Methods

**Reagents.** Porcine brain Arp2/3 complex, human GST-tagged N-WASP VCA domain, rabbit skeletal muscle actin, and ATP were purchased from Cytoskeleton. Tris base, CaCl<sub>2</sub>, TCEP, NaCl, KCl, MgCl<sub>2</sub>, and poly-L-lysine, and PEG 8000 were purchased from Sigma-Aldrich. Alexa Fluor 647 C2 maleimide was purchased from Thermo Fisher Scientific. Maleimide-Atto 488 and maleimide-Atto 594 were purchased from ATTO-TEC. Phalloidin-iFluor-488 and Arp2/3 inhibitor CK666 were purchased from Abcam. mPEG-SVA (MW 5000) was purchased from Laysan Bio.

A "cysteine-light" mutant form of human VASP was expressed from a pET vector (pET-6xHis-TEV-KCK-VASP(CCC-SSA)) that was a gift from Scott Hansen (31). Expression, purification, and cleavage of the His-tag from the VASP protein was conducted as explained previously (10). The resulting purified protein was stored in 25 mM HEPES pH 7.5, 200 mM NaCl, 5% glycerol, 1 mM EDTA, and 5 mM DTT. Single-use aliquots were flash frozen and stored at  $-80^{\circ}\text{C}$  until the day of an experiment.

**Protein Labeling.** The cysteine-light form of VASP allows for selective labeling of the single N-terminal cysteine using maleimide-conjugated dyes, as performed previously (31). Briefly, VASP was incubated with a threefold molar excess of dye for 2 h at room temperature to achieve a 10 to 20% labeling ratio. The protein was separated from the free dye by applying the labeling reaction to a Princeton CentriSpin-20 size exclusion column (Princeton Separations). Labeled VASP was eluted and stored in 50 mM Tris pH 7.8, 300 mM NaCl, 0.5 mM EDTA, 0.5 mM EGTA, and 5 mM TCEP. Monomeric actin was labeled on Cys-374 using maleimide-Atto 488. Dye was incubated with G-actin at a three to fivefold molar excess for 2 h at room temperature to achieve a labeling ratio of 20 to 30%. Unconjugated dye was separated from labeled actin by applying the labeling reaction to a Princeton CentriSpin-20 size exclusion column hydrated with A buffer (5 mM Tris-HCl pH 8, 0.2 mM CaCl<sub>2</sub>, 0.2 mM ATP, and 0.5 mM DTT). The eluted labeled protein was then centrifuged at 14k rpm for 15 min at 4  $^{\circ}\text{C}$  to remove aggregates, and flash-frozen

in single-use aliquots. VCA and Arp2/3 were labeled with maleimide Atto-488 and maleimide Atto-594, respectively, following the same protocol for VASP but with the following minor modifications (5, 21). Labeled VCA was eluted into 20 mM Tris pH 7.5, 25 mM KCl, 1 mM MgCl<sub>2</sub>, 0.5 mM EDTA, and 2% sucrose. Arp2/3 was eluted into 10 mM imidazole pH 7, 50 mM KCl, 1 mM MgCl<sub>2</sub>, 1 mM EGTA, 0.5 mM DTT, 100 μM ATP, and 5% sucrose. After labeling, both proteins were centrifuged at 21k rpm for 15 min at 4 °C to remove aggregates and used the same day.

**VASP Droplet Formation and Actin Polymerization.** VASP droplets were formed as described previously (10). Briefly, VASP was mixed with droplet buffer, 3% (w/v) PEG(8k) in 50 mM Tris pH 7.4, 150 mM NaCl, and 5 mM TCEP to the final concentrations stated in each experiment. PEG was added last to induce droplet formation. For experiments with Arp2/3 and VCA, these proteins were mixed with VASP in droplet buffer at the desired concentrations, and then PEG was added to induce droplet formation.

For droplet polymerization experiments with labeled monomeric actin, actin was added after the droplets were allowed to form for 10 min. Actin was allowed to polymerize in the droplets for 15 min, and then the droplets were imaged. For experiments with phalloidin-stained actin, unlabeled monomeric actin was added to preformed VASP droplets, allowed to polymerize for 15 min, and then phalloidin was added to stain the filaments for another 15 min before imaging.

**Microscopy.** Samples were prepared in wells formed by 1.5 mm thick silicone gaskets (Grace Biolabs) on Hellmanex II (Hellma) cleaned, no. 1.5 glass coverslips (VWR) passivated with poly-L-Lysine conjugated PEG5k. A second coverslip was placed on top to seal the imaging chamber to prevent evaporation during imaging. Fluorescence microscopy was performed using the Olympus SpinSR10 spinning disc confocal microscope fitted with a Hamamatsu Orca Flash 4.0V3 SCMOS Digital Camera. FRAP was performed using the Olympus FRAP unit 405-nm laser.

PLL-PEG was prepared as described previously with minor alteration (62). Briefly, amine-reactive mPEG-SVA was conjugated to Poly-L-Lysine (15-30 kD) at a molar ratio of 1:5 PEG to poly-L-lysine. The conjugation reaction was performed in 50 mM sodium tetraborate pH 8.5 solution and allowed to react overnight at room temperature with continued stirring. The product was buffer exchanged into PBS pH 7.4 using Zeba spin desalting columns (7K MWCO, ThermoFisher) and stored at 4 °C.

**Image Analysis.** ImageJ was used to quantify the distribution of droplet characteristics. Specifically, droplets were selected by thresholding in the VASP channel, and shape descriptors (e.g., diameter, aspect ratio), and protein intensities were measured using the analyze particles function.

FRAP data were analyzed using the FRAP Profiler plugin for ImageJ. Fluorescence recovery of a 2.5-μm diameter region was measured over time, and intensities were normalized to the maximum pre-bleach and minimum post-bleach intensity. All intensity data were corrected for photobleaching. Recovery was measured only for droplets of similar diameters.

Quantification of peripheral actin abundance was performed by scoring phalloidin-stained droplets for the presence of peripheral actin accumulation. Specifically, droplets were considered to have peripheral accumulation of actin if there was a decrease in actin fluorescence intensity in the center of the droplet, as verified by line profiles drawn across the droplet diameter. Droplets that had fused to other droplets were omitted. Droplets containing peripheral accumulation of filamentous actin were further classified based on their three-dimensional

arrangement of actin: either shells, rings, or discs, as performed previously (10). Rings, discs, and shells were differentiated by making 3D projections of each individual droplet. Shells were defined as spherical VASP droplets that have uniform spherical actin intensity in the 3D projection. Rings were defined as spherical VASP droplets that contained a planar arrangement of actin in the 3D projection. Discs were defined as non-spherical, planar droplets that colocalized both actin and VASP. Only droplets with peripheral accumulation of actin in the imaging plane were counted.

To calculate the partitioning of actin to the center of the droplet compared to the droplet periphery, the average intensity of a 15 x 15 pixel square in the center of the droplet was measured. This value was divided by the average intensity of the actin-rich ring formed at the droplet periphery to derive the relative enrichment in the center. The average intensity of the ring was measured by performing a radial transformation originating at the center of each droplet, and then measuring the average actin intensity along a line profile drawn in the center of each actin ring. All droplets analyzed were randomly selected.

To quantify the abundance of asters, images were scored for either rod-shaped droplets or aster-shaped droplets. Aster-droplets were defined as droplets with at least 4 actin-rich spokes radiating off of the central droplet core. Rods were defined as 2D linear droplets with VASP colocalized along the entire length. Droplets that intersected or overlapped with other droplets were not counted.

To calculate the partitioning of VASP and Arp2/3 to the aster-droplet spokes, the average intensities of the proteins in the spokes were divided by the average intensities in the droplet core, then normalized to the actin channel. Specifically, in a single z-slice in which the droplet core and spokes were in focus, the average intensities of Arp2/3, actin, and VASP in the droplet core were measured using ImageJ as mentioned above. To measure the intensity of proteins in the spokes, a circular line profile 1 μm from the surface of the droplet core was drawn, perpendicular to the spokes. Each intensity peak in the line profile corresponded to a spoke radiating off of the droplet. Using the actin channel as the reference for spoke peaks, the corresponding spoke intensities in the VASP and Arp2/3 channel were measured, and the resulting average spoke intensity was used to calculate the average spoke partitioning per droplet. Importantly, labeled VASP and Arp2/3 were used separately to avoid spectral overlap and bleed through.

**Data, Materials, and Software Availability.** All study data are included in the article and/or supporting information. The CytoSim source code, input files, analysis, and plotting scripts are available on GitHub ([https://github.com/achansek/CytoSim\\_VASP\\_Arp\\_VCA/](https://github.com/achansek/CytoSim_VASP_Arp_VCA/)) (63).

**ACKNOWLEDGMENTS.** This research was supported by grants from the NIH to J.C.S. (R35GM139531) and P.R. (R01GM132106), by the NSF through a Modulus Grant MCB 2327243 to P.R. and J.C.S., and by the Welch Foundation through Grant F-2047 to J.C.S. A.C. would like to acknowledge Dr. Francois Nedelec for feedback on the model schematic.

Author affiliations: <sup>a</sup>Department of Biomedical Engineering, University of Texas at Austin, Austin, TX 78712; <sup>b</sup>Department of Mechanical and Aerospace Engineering, University of California San Diego, La Jolla, CA 92093; <sup>c</sup>Department of Biochemistry and Structural Biology, University of Texas Health Science Center at San Antonio, San Antonio, TX 78229; and <sup>d</sup>Department of Chemical Engineering, University of Texas at Austin, Austin, TX 78712

1. L. Blanchoin, R. Boujemaa-Paterski, C. Sykes, J. Plastino, Actin dynamics, architecture, and mechanics in cell motility. *Physiol. Rev.* **94**, 235–263 (2014).
2. J. Stricker, T. Falzone, M. L. Gardel, Mechanics of the F-actin cytoskeleton. *J. Biomechanics* **43**, 9–14 (2010).
3. D. A. Fletcher, R. D. Mullins, Cell mechanics and the cytoskeleton. *Nature* **463**, 485–492 (2010).
4. P. K. Mattila, P. Lappalainen, Filopodia: Molecular architecture and cellular functions. *Nat. Rev. Mol. Cell Biol.* **9**, 446–454 (2008).
5. S. B. Padrick, L. K. Doolittle, C. A. Brautigam, D. S. King, M. K. Rosen, Arp2/3 complex is bound and activated by two WASP proteins. *Proc. Natl. Acad. Sci. U.S.A.* **108**, E472–E479 (2011).
6. P. Lappalainen, T. Kotila, A. Jégou, G. Romet-Lemonne, Biochemical and mechanical regulation of actin dynamics. *Nat. Rev. Mol. Cell Biol.* **23**, 836–852 (2022).
7. T. M. Svitkina *et al.*, Mechanism of filopodia initiation by reorganization of a dendritic network. *J. Cell Biol.* **160**, 409–421 (2003).
8. S. L. Gupton, F. B. Gertler, Filopodia: The fingers that do the walking. *Sci. STKE* **2007**, re5 (2007).
9. D. Vignjevic *et al.*, Role of fascin in filopodial protrusion. *J. Cell Biol.* **174**, 863–875 (2006).
10. K. Graham *et al.*, Liquid-like VASP condensates drive actin polymerization and dynamic bundling. *Nat. Phys.* **19**, 574–585 (2023), 10.1038/s41567-022-01924-1.
11. S. U. Setru *et al.*, A hydrodynamic instability drives protein droplet formation on microtubules to nucleate branches. *Nat. Phys.* **17**, 493–498 (2021).
12. N. H. Wubshet, Y. Bashirzadeh, A. P. Liu, Fascin-induced actin protrusions are suppressed by dendritic networks in giant unilamellar vesicles. *MBoC* **32**, 1634–1640 (2021).
13. J. Faix, K. Rottner, Ena/VASP proteins in cell edge protrusion, migration and adhesion. *J. Cell Sci.* **135**, jcs259226 (2022).
14. M. Krause, E. W. Dent, J. E. Bear, J. J. Loureiro, F. B. Gertler, Ena/VASP proteins: Regulators of the actin cytoskeleton and cell migration. *Annu. Rev. Cell and Dev. Biol.* **19**, 541–564 (2003).
15. K. W. Cheng, R. D. Mullins, Initiation and disassembly of filopodia tip complexes containing VASP and lamellipodin. *MBoC* **31**, 2021–2034 (2020).
16. K. Kühnel *et al.*, The VASP tetramerization domain is a right-handed coiled coil based on a 15-residue repeat. *Proc. Natl. Acad. Sci. U.S.A.* **101**, 17027–17032 (2004).

17. C. Bachmann, L. Fischer, U. Walter, M. Reinhard, The EVH2 domain of the vasodilator-stimulated phosphoprotein mediates tetramerization, F-actin binding, and actin bundle formation\*. *J. Biol. Chem.* **274**, 23549–23557 (1999).
18. C. P. Brangwynne, P. Tompa, R. V. Pappu, Polymer physics of intracellular phase transitions. *Nat. Phys.* **11**, 899 (2015).
19. M. T. Wei *et al.*, Phase behaviour of disordered proteins underlying low density and high permeability of liquid organelles. *Nat. Chem.* **9**, 1118–1125 (2017).
20. X. Su *et al.*, Phase separation of signaling molecules promotes T cell receptor signal transduction. *Science* **352**, 595–599 (2016).
21. J. Zalevsky, I. Grigorova, R. D. Mullins, Activation of the Arp2/3 complex by the *Listeria* ActA protein: ActA binds two actin monomers and three subunits of the Arp2/3 complex\*. *J. Biol. Chem.* **276**, 3468–3475 (2001).
22. F. Castellano, C. L. Clainche, D. Patin, M. F. Carlier, P. Chavrier, A WASp-VASP complex regulates actin polymerization at the plasma membrane. *EMBO J.* **20**, 5603–5614 (2001).
23. S. Havrylenko *et al.*, WAVE binds Ena/VASP for enhanced Arp2/3 complex-based actin assembly. *MBoC* **26**, 55–65 (2015).
24. X. J. Chen *et al.*, Ena/VASP proteins cooperate with the WAVE complex to regulate the actin cytoskeleton. *Dev. Cell* **30**, 569–584 (2014).
25. R. M. Welles *et al.*, Determinants of disordered protein co-assembly into discrete condensed phases. *bioRxiv [Preprint]* (2023). <https://doi.org/10.1101/2023.03.10.532134v1> (Accessed 29 September 2023).
26. E. D. Goley *et al.*, An actin-filament-binding interface on the Arp2/3 complex is critical for nucleation and branch stability. *Proc. Natl. Acad. Sci. U.S.A.* **107**, 8159–8164 (2010).
27. T. van Eeuwen *et al.*, Transition state of Arp2/3 complex activation by actin-bound dimeric nucleation-promoting factor. *Proc. Natl. Acad. Sci. U.S.A.* **120**, e2306165120 (2023).
28. L. M. Machesky, R. H. Insall, Scar1 and the related Wiskott-Aldrich syndrome protein, WASP, regulate the actin cytoskeleton through the Arp2/3 complex. *Curr. Biol.* **8**, 1347–1356 (1998).
29. Q. Luan, A. Zelter, M. J. MacCoss, T. N. Davis, B. J. Nolen, Identification of Wiskott-Aldrich syndrome protein (WASP) binding sites on the branched actin filament nucleator Arp2/3 complex. *Proc. Natl. Acad. Sci. U.S.A.* **115**, E1409–E1418 (2018).
30. U. D. Carl *et al.*, Aromatic and basic residues within the EVH1 domain of VASP specify its interaction with proline-rich ligands. *Curr. Biol.* **9**, 715–718 (1999).
31. S. D. Hansen, R. D. Mullins, VASP is a processive actin polymerase that requires monomeric actin for barbed end association. *J. Cell Biol.* **191**, 571–584 (2010).
32. S. Banjade, M. K. Rosen, Phase transitions of multivalent proteins can promote clustering of membrane receptors. *Elife* **3**, e04123 (2014).
33. P. Li *et al.*, Phase transitions in the assembly of multivalent signalling proteins. *Nature* **483**, 336–340 (2012).
34. Y. Ideses, Y. Brill-Karniely, L. Haviv, A. Ben-Shaul, A. Bernheim-Groswasser, Arp2/3 branched actin network mediates filopodia-like bundles formation in vitro. *PLoS One* **3**, e3297 (2008).
35. L. Blanchoin *et al.*, Direct observation of dendritic actin filament networks nucleated by Arp2/3 complex and WASP/Scar proteins. *Nature* **404**, 1007–1011 (2000).
36. H. N. Higgs, L. Blanchoin, T. D. Pollard, Influence of the C terminus of Wiskott-Aldrich Syndrome Protein (WASP) and the Arp2/3 complex on actin polymerization. *Biochemistry* **38**, 15212–15222 (1999).
37. B. Hetrick, M. S. Han, L. A. Helgeson, B. J. Nolen, Small molecules CK-666 and CK-869 inhibit actin-related protein 2/3 complex by blocking an activating conformational change. *Chem. Biol.* **20**, 701–712 (2013).
38. B. J. Nolen *et al.*, Characterization of two classes of small molecule inhibitors of Arp2/3 complex. *Nature* **460**, 1031–1034 (2009).
39. R. D. Mullins, J. A. Heuser, T. D. Pollard, The interaction of Arp2/3 complex with actin: Nucleation, high affinity pointed end capping, and formation of branching networks of filaments. *Proc. Natl. Acad. Sci. U.S.A.* **95**, 6181–6186 (1998).
40. C. H. Schreiber, M. Stewart, T. Duke, Simulation of cell motility that reproduces the force-velocity relationship. *Proc. Natl. Acad. Sci. U.S.A.* **107**, 9141–9146 (2010).
41. A. Chandrasekaran, E. Giniger, G. A. Papoian, Nucleation causes an actin network to fragment into multiple high-density domains. *Biophys. J.* **121**, 3200–3212 (2022).
42. F. Gittes, B. Mickey, J. Nettleton, J. Howard, Flexural rigidity of microtubules and actin filaments measured from thermal fluctuations in shape. *J. Cell Biol.* **120**, 923–934 (1993).
43. A. E. Cohen, L. Mahadevan, Kinks, rings, and rackets in filamentous structures. *Proc. Natl. Acad. Sci. U.S.A.* **100**, 12141–12146 (2003).
44. N. H. Wubshet, Y. Bashirzadeh, A. P. Liu, Fascin-induced actin protrusions are suppressed by dendritic networks in giant unilamellar vesicles. *MBoC* **32**, 1634–1640 (2021).
45. D. Vignjevic *et al.*, Formation of filopodia-like bundles in vitro from a dendritic network. *J. Cell Biol.* **160**, 951–962 (2003).
46. L. Haviv *et al.*, Reconstitution of the transition from lamellipodium to filopodium in a membrane-free system. *Proc. Natl. Acad. Sci. U.S.A.* **103**, 4906–4911 (2006).
47. Y. Brill-Karniely, Y. Ideses, A. Bernheim-Groswasser, A. Ben-Shaul, From branched networks of actin filaments to bundles. *Chem. Eur. J. Chem. Phys.* **10**, 2818–2827 (2009).
48. A. Schirenbeck *et al.*, The bundling activity of vasodilator-stimulated phosphoprotein is required for filopodium formation. *Proc. Natl. Acad. Sci. U.S.A.* **103**, 7694–7699 (2006).
49. V. Laurent *et al.*, Role of proteins of the Ena/VASP family in actin-based motility of *Listeria monocytogenes*. *J. Cell Biol.* **144**, 1245–1258 (1999).
50. T. D. Pollard, L. Blanchoin, R. D. Mullins, Molecular mechanisms controlling actin filament dynamics in nonmuscle cells. *Annu. Rev. Biophys. Biomol. Struct.* **29**, 545–576 (2000).
51. L. Yang, D. Sept, A. E. Carlsson, Energetics and dynamics of constrained actin filament bundling. *Biophys. J.* **90**, 4295–4304 (2006).
52. A. P. Liu *et al.*, Membrane-induced bundling of actin filaments. *Nat. Phys.* **4**, 789–793 (2008).
53. M. Krause, A. Gautreau, Steering cell migration: Lamellipodium dynamics and the regulation of directional persistence. *Nat. Rev. Mol. Cell Biol.* **15**, 577–590 (2014).
54. D. Breitsprecher *et al.*, Clustering of VASP actively drives processive, WH2 domain-mediated actin filament elongation. *EMBO J.* **27**, 2943–2954 (2008).
55. S. Bruhmann *et al.*, Distinct VASP tetramers synergize in the processive elongation of individual actin filaments from clustered arrays. *Proc. Natl. Acad. Sci. U.S.A.* **114**, E5815–E5824 (2017).
56. J. D. Winkelman, C. G. Bilancia, M. Peifer, D. R. Kovar, Ena/VASP Enabled is a highly processive actin polymerase tailored to self-assemble parallel-bundled F-actin networks with Fascin. *Proc. Natl. Acad. Sci. U.S.A.* **111**, 4121–4126 (2014).
57. D. A. Applewhite *et al.*, Ena/VASP proteins have an anti-capping independent function in filopodia formation. *Mol. Biol. Cell.* **18**, 2579–2591 (2007).
58. T. Pokrant *et al.*, Ena/VASP clustering at microspike tips involves lamellipodin but not I-BAR proteins, and absolutely requires unconventional myosin-X. *Proc. Natl. Acad. Sci. U.S.A.* **120**, e2217437120 (2023).
59. S. B. Padrick *et al.*, Hierarchical regulation of WASP/WAVE proteins. *Mol. Cell* **32**, 426–438 (2008).
60. Y. Sun *et al.*, Switch-like Arp2/3 activation upon WASP and WIP recruitment to an apparent threshold level by multivalent linker proteins in vivo. *Elife* **6**, e29140 (2017).
61. T. Nast-Kolb, P. Bleicher, M. Payr, A. R. Bausch, VASP localization to lipid bilayers induces polymerization driven actin bundle formation. *MBoC* **33**, ar91 (2022).
62. W. F. Zeno *et al.*, Synergy between intrinsically disordered domains and structured proteins amplifies membrane curvature sensing. *Nat. Commun.* **9**, 4152 (2018).
63. A. Chandrasekaran, K. Graham, J. Stachowiak, P. Rangamani, Supplemental code/replication data. GitHub. [https://github.com/achansek/CytoSim\\_VASP\\_Arp\\_VCA](https://github.com/achansek/CytoSim_VASP_Arp_VCA). Deposited 29 September 2023.